Chemical Engineering Journal 489 (2024) 151227

Contents lists available at ScienceDirect

Chemical Engineering Journal

journal homepage: www.elsevier.com/locate/cej

Ca^{2+} induced highly fluorescent $CsPb(Br/Cl)_3$ perovskite quantum dots via fast Anion-Exchange & Cation-Doping Inter-Promotion strategy for efficient deep-blue light-emitting diodes

Jing Zhou [a,b,c], Hongli Liu [a,c,*], Sisi Wang [b], Longfei Yuan [a,c], Narjes Dridi [b], Shirong Wang [a,c], Hedi Mattoussi [b,*], Xianggao Li [a,c,*]

[a] School of Chemical Engineering and Technology, Tianjin University, Tianjin 300072, China
[b] Department of Chemistry and Biochemistry, Florida State University, Tallahassee, FL 32306, USA
[c] Collaborative Innovation Center of Chemical Science and Engineering (Tianjin), Tianjin 300072, China

ARTICLE INFO

Keywords:
Deep-blue
PeLEDs
$CaBr_2$ doping
Mixed halide
Ultrafast ion-exchange

ABSTRACT

Despite the impressive development of perovskite light-emitting diodes (PeLEDs), it is still challenging to achieve high-efficiency deep-blue PeLEDs using colloid perovskite quantum dots (PQDs). The efficiency of PQDs with a wavelength below 460 nm, which meets the requirements for deep-blue emission in the Telecommunication Union UHD television standard (ITU REC. 2020), lags far behind those of their sky-blue counterparts. To address this issue, a novel strategy of fast anion-exchange & cation-doping inter-promotion (**FAECDIP**) is proposed to achieve highly efficient deep-blue PQDs by introducing $CaBr_2$ into the $CsPbCl_3$ PQDs. Owing to the presence of Ca^{2+}, the speed of ion exchange is increased, driven by the smaller cation, Ca^{2+}, improving the preparation efficiency. Additionally, Ca^{2+} was doped on the surface of PQDs. Based on studies of fast anion-exchange and theoretical calculations, Ca^{2+} improves the optical performance by decreasing the number of traps and increasing the crystallinity of target PQDs, facilitating the stability of treated films and PeLEDs by enhancing the formation energy of halogen vacancies. Here, a high PLQY of 80.3 % $CaBr_2$-induced $CsPb(Cl/Br)_3$ deep-blue PQDs (~446 nm) was achieved. The correspondent PeLEDs (~447 nm) achieved a superior EQE of 5.88 %, which is the state-of-the-art among the reported deep-blue PeLEDs. Our strategy provides a potential route to achieve deep-blue PeLEDs, which differs from the previous tedious-complex methods.

1. Introduction

All-inorganic $CsPbX_3$ (X = Cl, Br, and I) perovskite quantum dots (PQDs) are widely acknowledged to be some of the most promising candidates for next generation display applications because of their high photoluminescence quantum yield (PLQY), and their tunable and narrow emission profiles.[1–6] Lots of exploration on improving the performance of display primary colors (red, green, and blue) have been conducted.[7–10] With the great efforts recently, the maximum external quantum efficiency (EQE) of green perovskite light-emitting diodes (PeLEDs) has leaped to 30.84 %[10], and the maximum efficiency of red PeLED has also exceeded 25 %[11]. However, both the efficiency and stability of blue PeLEDs still lag far behind those of their green and red counterparts, especially in deep-blue regions with emissions lower than 460 nm.[12–17] Among the currently reported ultra-deep-blue PeLEDs with the Commission Internationale de L'Eclairage (CIE) (0.131, 0.046) of Telecommunication Union Ultra High Definition (UHD) television standard (ITU REC. 2020), the EQEs barely exceed 5 %.[16] To realize high color gamut display, fruitful research on deep-blue PQD materials is still necessary for new generation display technologies.

Common approaches that develop large band gap $CsPbX_3$ nanocrystals (NCs) with deep-blue emission have deserved exploration, including growing two-dimensional (2D) perovskite nanostructures (*e.g.* nanoplatelets),[17–21] doping divalent cations into NC structure, [21–29] or exploring mixed Cl/Br halide core PQDs. [29–38] PeLEDs based on low-dimensional PQDs have achieved some good results, however, deficient carrier injection caused by the excessive organic ligands typically restricts the progress of low-dimensional NCs in 2D or quasi-2D devices. To date, the record EQE of deep-blue PeLED is 4.62 % (~457 nm) obtained by dimension reduction perovskite NCs with the

* Corresponding authors.
E-mail addresses: liuhongli@tju.edu.cn (H. Liu), hmattoussi@fsu.edu (H. Mattoussi), lixianggao@tju.edu.cn (X. Li).

https://doi.org/10.1016/j.cej.2024.151227
Received 3 January 2024; Received in revised form 8 April 2024; Accepted 10 April 2024
Available online 16 April 2024

assistance of phenyl butylamine and ethylamine.[16] Further improving the EQE of deep-blue PeLEDs is urgent, especially using a facile controllable method. Modulating mixed halide PQDs is another route to obtain deep-blue emitting PeLED. Yang's group prepared $CsPb(Cl/Br)_3$ PQDs and gained deep-blue PeLEDs with an EQE of 3.66 % at 460 nm.[37] Whereas, the only major issue could be the poor spectrum stability which will greatly decrease the optical performance of PeLEDs based on mixed halide PQDs. To address this issue, Gao and colleagues reported PeLED with Cu^{2+}-doped $CsPb(Cl/Br)_3$ effectively inhibited the ion-migration compared with the undoped PQDs and demonstrated stable electroluminescence (EL) at 462 nm with no shift under varied voltages from 5 to 8 V.[22] Moreover, cation dopants such as Ni^{2+},[38] Mn^{2+},[23] La^{3+},[39] and Ca^{2+}[40] can enhance the optical properties and structural stability of $CsPb(Cl/Br)_3$ PQDs are known and deserves deep consideration. Generally, the preparation of cation doping and halide-mixing is explored separately, which complicates the preparation process. To simplify the process of preparing PQDs, simultaneous ion exchange and cation doping were used to obtain deep-blue PQDs. Huang developed post-synthetic doping of $MnCl_2$ molecules into preformed $CsPbBr_3$ perovskite nanocrystals via a halide exchange-driven cation exchange.[41] However, Mn^{2+} induced a bi-emission peak. Zhang *et al.* used calcium halide and ammonium ions simultaneously to modify the $CsPb(Br/Cl)_3$ NCs in situ to reduce surface defects, finally remarkably enhancing the photoluminescence quantum yield (PLQY) from 13 % to 93 % with an emission peak at 455 nm.[40] Even this strategy can only optimize PQDs with one wavelength, not continuous spectral tunability at a time, Ca^{2+}-doped $CsPb(Br/Cl)_3$ NCs still show great potential for the preparation of devices.

To fill the gap of Ca^{2+}-doped $CsPb(Br/Cl)_3$ PQDs in applications, blue emitting Ca^{2+}-doped $CsPb(Br/Cl)_3$ PQDs were prepared by **FAECDIP**. It is an approach that involves doping calcium into the lead vacancies of the nanocrystal structure through ion exchange, while the doped Ca^{2+} triggers rapid anion exchange. Here, Ca^{2+}-doping and halide exchange were motivated by two facts: a suitable ionic radius of Ca^{2+} and a favorable bond dissociation energy (BDE) of Ca-Br. Fortunately, this route achieved a fast ion exchange different from Huang's[41] work. Additionally, the deep-blue emitting Ca^{2+}-doped $CsPb(Cl/Br)_3$ PQDs obtained by fast halide ion-exchange and Ca^{2+} doping occur simultaneously. Results demonstrated that Ca^{2+} was successfully incorporated into the surface crystal lattice by halide substitution. The difference between **FAECDIP** and traditional doping is that doping and fast ion-exchange are interlocking processes by this method, instead of a one-

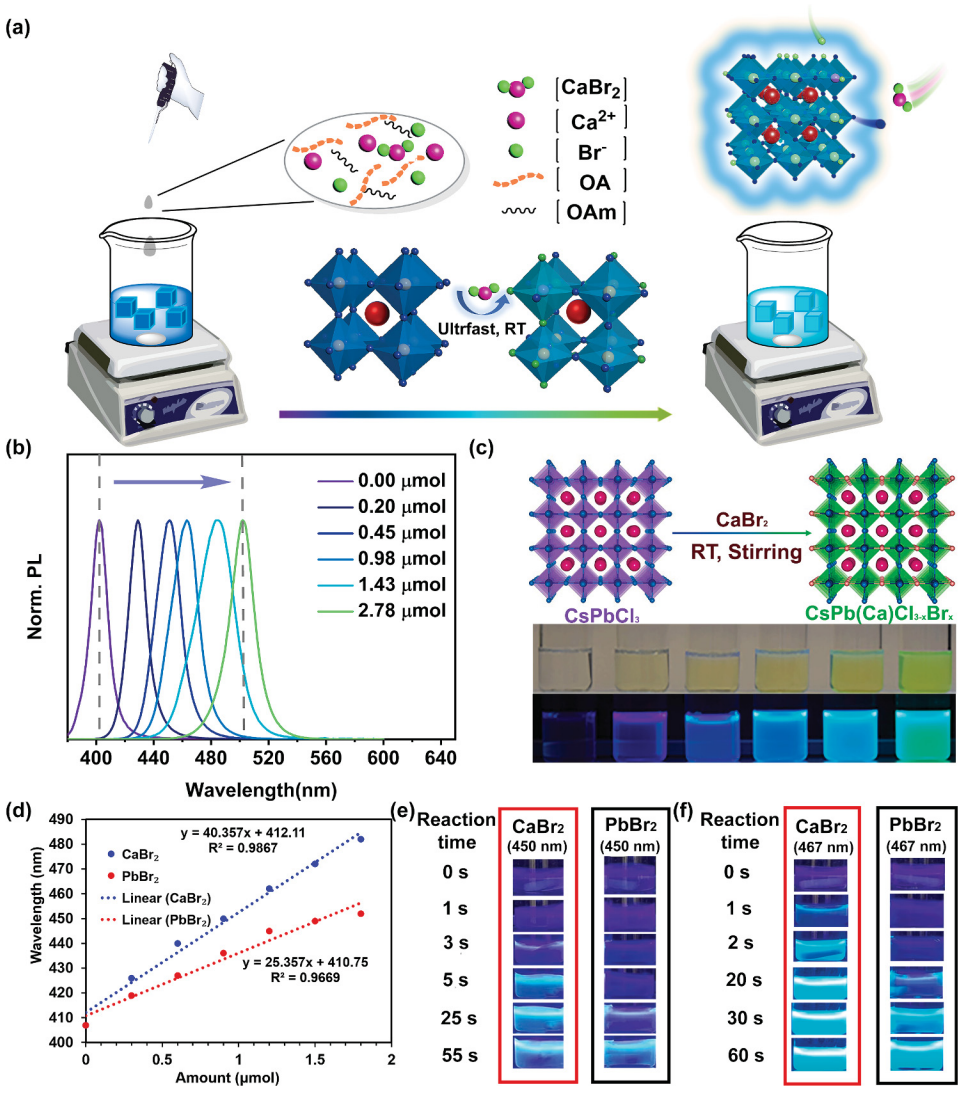

Fig. 1. (a) Diagram of $CaBr_2$-$CsPb(Cl/Br)_3$ PQDs preparation and fast ion-exchange process. (b) PL emission spectra of $CsPbCl_3$ PQDs regulated by $CaBr_2$ from 402 to 500 nm and (c) corresponding photos under daylight and UV. (d) Linear fitting of the amount and wavelength for adding $CaBr_2$ (~430, 440, 450, 462, 472 and 482 nm) and $PbBr_2$ (~419, 427, 436, 445, 449 and 452 nm). Photos of PQD dispersions' PL change with time after adding calcium salt, whose emission wavelength are located at (e) 450 nm and (f) 470 nm.

pot method or prolonged molecular diffusion. **FAECDIP** not only permits an impressive PLQY but also enables continuous spectral tunability, and it is simpler and more convenient compared with the previous contributions. Target Ca^{2+}-doped $CsPb(Cl/Br)_3$ PQDs can realize tunable photoluminescence (PL) ranging from 430 ~ 470 nm by adjusting the amount of $CaBr_2$. Among them, deep-blue $CaBr_2$-$CsPb(Cl/Br)_3$ PQDs exhibited a maximum PLQY of 80.3 % at 446 nm. Correspondingly, this PeLED was endowed with deep-blue emission at 447 nm with the EQE of 5.88 % and CIE coordinates of (0.158, 0.018), which is the record value among the reports with deep-blue PeLED. Meanwhile, the EL spectral of $CaBr_2$-$CsPb(Cl/Br)_3$ PeLED is relatively stable under the applied voltage from 4 to 7 V.

2. Result and discussion

2.1. FAECDIP evolution of $CaBr_2$-$CsPb(Cl/Br)_3$ PQDs

The procedure is schematically demonstrated in Fig. 1**a**. $CsPbCl_3$ PQDs were grown via the hot-injection method reported by Kovalenko and co-workers.[42] $CaBr_2$ solution was prepared by dissolving the salt in hexane premixed with oleic acid (OA) and oleylamine (OLA) ligands. It is the source of both cation-doping (Ca^{2+}) and anion-exchange (Br^-). Soluble Br^- rapidly exchanges with Cl^- in $CsPbCl_3$ PQDs yielding a mixed halide core composition PQDs and Ca^{2+} repairs the surface Pb vacancies. The resulting PQD is denoted as $CaBr_2$-$CsPb(Cl/Br)_3$. As shown in Fig. 1**b, c**, the fluorescence spectra collected from dispersions of $CaBr_2$-$CsPb(Cl/Br)_3$ PQDs exhibit a redshift from 410 to 500 nm with the addition of $CaBr_2$. Notably, the reversible regulation of the PQDs from green to blue and even violet can also be realized with this strategy just by adding $CaCl_2$ solution to the pre-synthesized $CsPbBr_3$ PQDs (**Fig. S1**). The interesting phenomenon observed in this study is that introducing Ca^{2+} can achieve fast ion-exchange. Furthermore, the forward tuning process is always faster and more efficient than the backward process. This could be possibly explained by the BDE theory. Accordingly, the smaller the difference in BDE values, the faster the ion-exchange will occur. Here, the BDE value difference of Ca-Br (~339 KJ mol^{-1}) and Pb-Cl (~301 KJ mol^{-1}) is less than that of Ca-Cl (~409 KJ mol^{-1}) and Pb-Br (~236 KJ mol^{-1}).[43,44] Although rapid ion-exchange can be explained by BDE theory, the interaction between Ca^{2+} and ion-exchange processes is still worthy of further investigation.

To reveal the effect of ion-exchange process on the amount of Ca^{2+}-introduced, Inductively Coupled Plasma-Optical Emission-Spectrometry (ICP-OES) was used to calibrate the molar ratio of Ca to Pb. Here, calcium acetate ($Ca(CH_3COO)_2$) was introduced into $CsPb(Cl/Br)_3$ PQDs as a control without anion-exchange process and detailed preparation is supplied in **Supporting Information (SI)**. Meanwhile, $CaBr_2$-$CsPb(Cl/Br)_3$ PQDs with the same emission peak were obtained. **Table S1** summarizes the measured Ca and Pb amounts via ICP-OES for $Ca(CH_3COO)_2$ and $CaBr_2$ treated $CsPb(Cl/Br)_3$ PQDs, the corresponding element ratio ([Ca]/[Pb]) are 2.19 % and 2.26 %, respectively. It illustrates that Ca^{2+}-doping is a relatively small doping process.

To clarify this, $CaBr_2$-driven fast ion-exchange phenomenon, the crystal growth kinetics of $CaBr_2$-$CsPb(Cl/Br)_3$ PQDs deserve deep study and discussion. For reference, the as-grown $CsPbCl_3$ PQDs were also incubated with a solution of $PbBr_2$ dissolved with hexane containing a mixture of OA and OLA as above. The resulting NC are denoted as $PbBr_2$-$CsPb(Cl/Br)_3$ PQDs. During the ion-exchange reaction, **Fig. S2** indicates that less $CaBr_2$ compared to $PbBr_2$ was needed to obtain $CaBr_2$-$CsPb(Cl/Br)_3$ PQDs with desired emission. For example, when 0.9 μmol $PbBr_2$ was added into 1 mL $CsPbCl_3$ PQD solution to adjust the PL peak to 454 nm, only 0. 45 μmol $CaBr_2$ was required to achieve the emission of 453 nm. The molar ratio of $PbBr_2$: $CaBr_2$ is ~ 2 and is constant to achieve the same target emission wavelength. This demonstrates that the ion-exchange reaction of $CaBr_2$ has higher reaction efficiency than those induced by $PbBr_2$, which is attributed to the theory that close BDE values favor ion-exchange (illustrated in **Fig. S3**). It is known that ion-exchange rates are affected by diffusion. In our modeling, anion-exchange promotes Ca^{2+}-doping owing to Ca^{2+} bearing a smaller ionic radius and diffusing into the PQDs structure faster than Pb^{2+}, speeding up the anion-exchange rate. To further verify this hypothesis, the same amount of $CaBr_2$ and $PbBr_2$ (0.27, 0.54, 0.81, 1.08, 1.35, 1.62 μmol) was respectively added to $CsPbCl_3$ PQD solutions to evaluate their PL. As revealed in Fig. 1**d**, the obtained $PbBr_2$-$CsPb(Cl/Br)_3$ PQDs suffer weaker redshift than $CaBr_2$-$CsPb(Cl/Br)_3$ PQDs. This indicates that $CaBr_2$ causes more Br substitution than that of $PbBr_2$. Moreover, the PL peak position of ion-exchanged $CsPb(Cl/Br)_3$ PQDs demonstrates a perfect positive linear dependency on the molar amount of $CaBr_2$ and $PbBr_2$. A slope of 40.357 and 25.357 nm/μmol is respectively obtained by $CaBr_2$-$CsPb(Cl/Br)_3$ and $PbBr_2$-$CsPb(Cl/Br)_3$ PQDs, revealing that $CaBr_2$ gives a sharper redshift increase than $PbBr_2$. Based on the fitting, it can be roughly calculated that the reaction rate of $CaBr_2$ is ~ 1.6 times higher than that of $PbBr_2$ in promoting halide exchange reaction.

Besides the reactant amount, the speed of the ion-exchange reaction was also explored. The PL of $CaBr_2$-$CsPb(Cl/Br)_3$ and $PbBr_2$-$CsPb(Cl/Br)_3$ PQDs respectively tuned to 450 and 467 nm were traced by recording a video under the illumination of UV-lamp to monitor their emission change. As revealed in Fig. 1**e, f**, anion-exchange of $CaBr_2$-treated $CsPbCl_3$ PQDs was completed in several seconds (~10 s), while the one with $PbBr_2$ took almost 1 min (the complete video can be found in **SI**). Additionally, the PL profiles of the associated PQDs were monitored during the ion-exchange process every few seconds. As plotted in Fig. S4**a,** $PbBr_2$-$CsPb(Cl/Br)_3$ PQDs with a gradual redshift were recorded from 410 to 465 nm within 75 s, and meanwhile, asymmetric peaks were collected in the intermediate state. For $CaBr_2$-$CsPb(Cl/Br)_3$ PQDs, the first plot has already fully shifted to 470 nm and after that, the emission has a slight blue shift to 465 nm (see Fig. S4**b**). It can be ascribed to that ion-exchange induced by $CaBr_2$ can occur rapidly (within a few seconds), which is drastically faster than that with $PbBr_2$. Overall, it has been experimentally shown that $CaBr_2$ does facilitate the ion-exchange reaction efficiency (requiring less reactant) as well as a faster reaction speed than $PbBr_2$. Consequently, this facile strategy namely **FAECDIP** permits the realization of blue-emitting PQDs. The optical and structural properties of the obtained PQDs by **FAECDIP** need further characterization.

2.2. Characterization of $CaBr_2$-$CsPb(Cl/Br)_3$ PQDs

Here, three sets of $CaBr_2$-$CsPb(Cl/Br)_3$ PQDs with emission around 430, 450, and 467 nm were obtained, while $PbBr_2$-$CsPb(Cl/Br)_3$ PQDs were also prepared as a reference. The samples were respectively denoted as Ca_{-430}, Ca_{-450}, Ca_{-467}, Pb_{-430}, Pb_{-450} and Pb_{-467} (The subscript corresponds to the wavelength). UV–visible absorption and PL spectra of those PQDs are plotted in Fig. 2**a**. It can be observed that the absorption profiles of $CaBr_2$-$CsPb(Cl/Br)_3$ and $PbBr_2$-$CsPb(Cl/Br)_3$ PQDs match very well, indicative of a preserved structural integrity of nanocrystals with Ca^{2+} doping. However, the PL profiles of $CaBr_2$-$CsPb(Cl/Br)_3$ PQDs have higher emission signals, with intensity increases 40x times for Ca_{-430}, 15x for Ca_{-449}, and 5x for Ca_{-467} compared to their $PbBr_2$-$CsPb(Cl/Br)_3$ counterparts. The fluorescence images of those dispersions shown in Panel 2a (inset) provide a visual rendition of the PL increase. The corresponding PL lifetime profiles are plotted in Fig. 2**b**, which indicates that exciton lifetimes measured for the $CaBr_2$-$CsPb(Cl/Br)_3$ PQD dispersions are longer than those measured for the $PbBr_2$-$CsPb(Cl/Br)_3$ PQD samples. Fig. 2**c** demonstrates a side-by-side comparison between the PLQY values (measured using an integrating sphere) for dispersions of $CaBr_2$-$CsPb(Cl/Br)_3$ and $PbBr_2$-$CsPb(Cl/Br)_3$ PQDs with emission peaks centered at ~ 420, ~ 430, ~ 440, ~ 450, ~ 460 and ~ 470 nm. Sample concentration was determined using UV absorption test and hexane was used as a blank control. The optical density values of all the sample excitation wavelengths (365 nm) are normalized below 0.1 to ensure the accuracy of the measurements. The data shows that there is a higher PLQY measured for the $CaBr_2$-$CsPb(Cl/Br)_3$ PQDs compared to

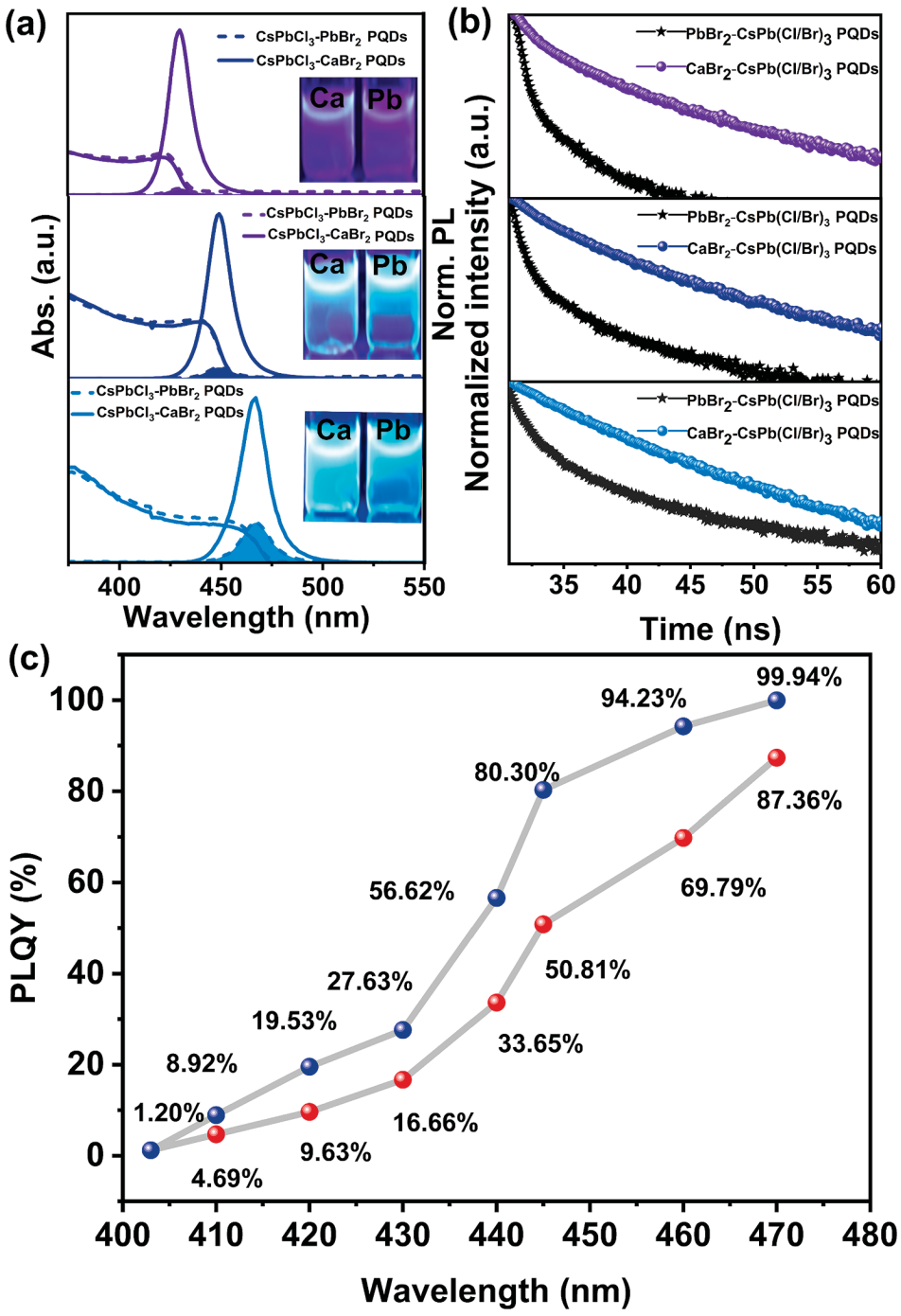

Fig. 2. (a) Superimposed absorption and emission spectra of Ca_{-430}, Ca_{-450}, Ca_{-467} together with Pb_{-430}, Pb_{-450} and Pb_{-467} dispersions. (b) Time-resolved PL profiles measured for $CaBr_2$-$CsPb(Cl/Br)_3$ PQDs side-by-side with $PbBr_2$-$CsPb(Cl/Br)_3$. Samples with emission wavelengths at 430, 449 and 467 nm are shown. (c) PLQY of $CsPb(Cl/Br)_3$ PQD samples with emission tuned using treatment with $CaBr_2$ and $PbBr_2$. The emission wavelengths of the samples are 410, 420, 430, 445, 460, and 468 nm.

the $PbBr_2$-$CsPb(Cl/Br)_3$ samples throughout the whole range of wavelengths probed. This is due to better passivation of defects in $CaBr_2$-$CsPb(Cl/Br)_3$ PQDs group. This increase is consistent with the longer PL lifetimes of $CaBr_2$-$CsPb(Cl/Br)_3$ dispersion compared to that of $PbBr_2$.

To shed light on how Ca^{2+} cations are integrated with the PQD and the reason that the optical properties of $CaBr_2$-$CsPb(Cl/Br)_3$ are superior to that of $PbBr_2$-$CsPb(Cl/Br)_3$ PQDs, the crystal structure and the morphology of $CaBr_2$-$CsPb(Cl/Br)_3$ PQD are characterized using powder X-ray diffraction (PXRD) and high-angle annular dark-field scanning transmission electron microscopy (HAADF-STEM). PXRD patterns were collected for the three sets of blue-emitting $CaBr_2$-$CsPb(Cl/Br)_3$ PQDs, namely, Ca_{-430}, Ca_{-450}, and Ca_{-467}. The powder patterns in Fig. 3**a** reveal that all three $CaBr_2$-$CsPb(Cl/Br)_3$ PQDs maintain the structure of Cl-based parent PQDs, and the structure matches the published PDF: mp-23037. Focusing on the angle region $2\theta = 15 - 35^{\circ}$, the patterns show that the diffraction peaks emanating from the (100) to (210) crystal planes exhibit progressive shifts to lower angles. It indicates the expansion of the interplanar crystal spacing (due to a change in the crystal unit cell) caused by partial Cl^- to Br^- substitution following incubation and the reaction of the nanocrystals with $CaBr_2$. This is also

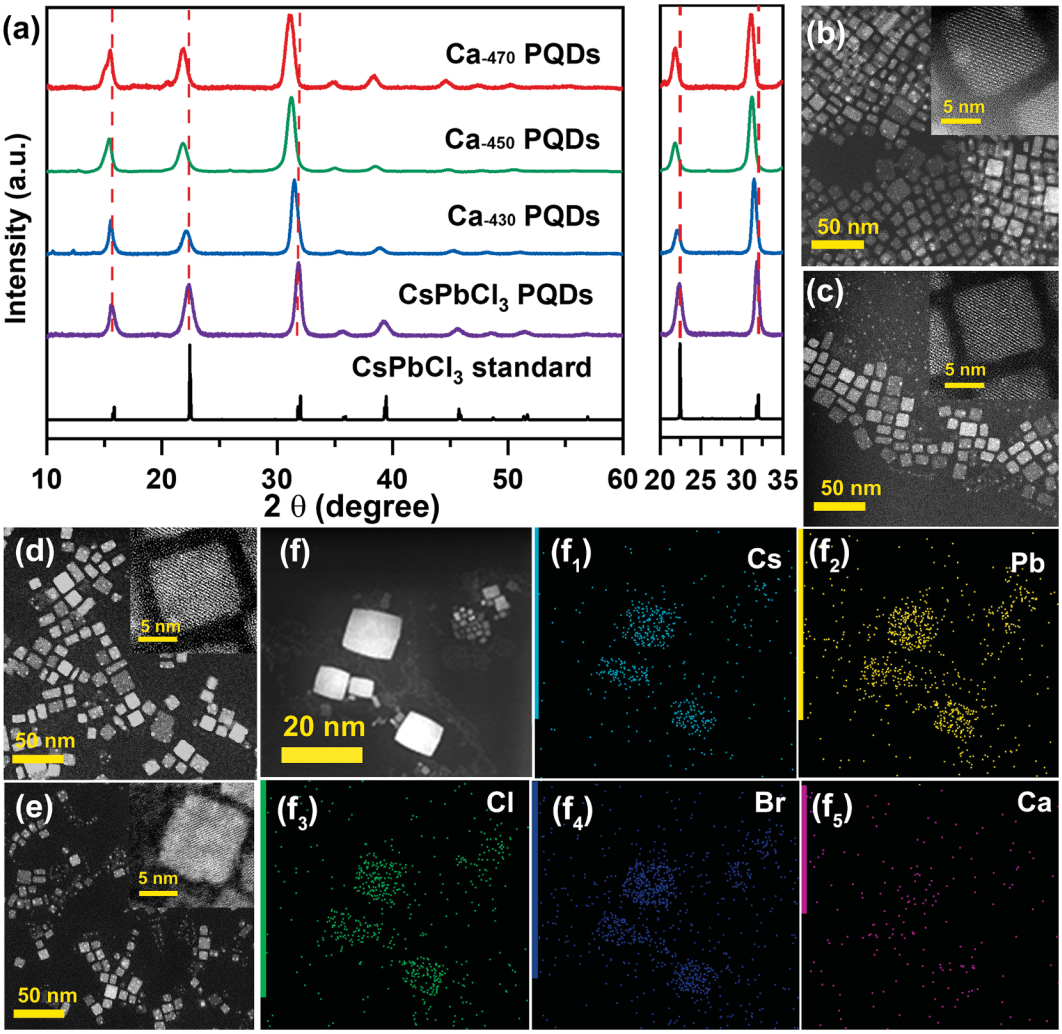

Fig. 3. (a) Powder XRD patterns collected from a standard $CsPbCl_3$ PQDs, side-by-side with the those of $CaBr_2$-passivated $CsPb(Cl/Br)_3$ (Ca_{-430}, Ca_{-450} and Ca_{-470}) along with the standard pattern of bulk $CsPbCl_3$ (**JCPDF: 84–0438**). STEM images of (b) $CsPbCl_3$, (c) Ca_{-430}, (d) Ca_{-450} and (e) Ca_{-467}. (f) TEM and element mapping of the sample Ca_{-450}.

reflected in the red shift in the PL acquired from samples with a higher fraction of Br^-. To evaluate whether Ca^{2+} ions are primarily located at the surfaces or integrated into the nanocrystal cores, PQDs emitting at 431 nm were prepared via the treatment of $CsPbCl_3$ with either $CaBr_2$ or $PbBr_2$. This excludes the effects of the halide ions source used. The diffraction patterns exhibit only marginal shifts in the measured peaks. In particular, the peak resulting from diffraction of the (200) planes shifts from 31.54° for $CaBr_2$-$CsPb(Cl/Br)_3$ PQDs to 31.66° for $PbBr_2$-$CsPb(Cl/Br)_3$ PQDs (see **Fig. S5**). This corresponds to a change in the interplanar lattice distance from 4.0176 Å for $PbBr_2$-$CsPb(Cl/Br)_3$ PQDs to 4.0145 Å for $CaBr_2$-$CsPb(Cl/Br)_3$ PQDs. This small change is not large enough to support a substantial core intake of Ca^{2+}. Therefore, Ca^{2+} is more likely to act on the surface of PQDs. **Fig. S6** compares the diffraction peak intensity of $CaBr_2$-$CsPb(Cl/Br)_3$ and $PbBr_2$-$CsPb(Cl/Br)_3$ PQDs with 431 nm emission wavelength. It shows that these two samples remain in the same diffraction peak positions, indicating that they acquired the same emission wavelength. However, the diffraction peak intensity of $CaBr_2$-$CsPb(Cl/Br)_3$ in the 10 ~ 25° angular region of 2θ is higher than that of $PbBr_2$-$CsPb(Cl/Br)_3$ PQDs, which reveals higher crystallinity of (100) and (110) planes. Combined with the role of Ca^{2+} acting on the surface of PQDs and based on the report that XRD diffraction peak intensity of PQDs to be changed by B-site doping,[45] Ca^{2+} successfully participated in the B-site doping on the surface of PQDs.

To further confirm that Ca^{2+} interacts with PQDs, high resolution HAADF-STEM measurements were conducted to investigate these samples of $CaBr_2$-$CsPb(Cl/Br)_3$ PQDs. Fig. 3**b** demonstrates the cubic form and average edge length (~8.3 nm) of the as-grown $CsPbCl_3$ PQDs. Nevertheless, a distinct trend in the growth of the nanocube edge size as the $CaBr_2$ concentration increases was observed (Fig. 3**c–e**). The average edge length of $CaBr_2$-$CsPb(Cl/Br)_3$ PQDs rises from 8.3 to 9.5, 9.6, and 9.7 nm because of a considerable replacement of small Cl^- ions (1.81 Å) with large Br^- ions (1.96 Å), matching with $CsPbCl_3$, Ca_{-430}, Ca_{-450} and Ca_{-466} PQDs as seen in **Fig. S7**. EDS examination of Ca_{-450} PQDs shows the distribution of the Cs (Fig. 3**f1**), Pb (Fig. 3**f2**), Cl (Fig. 3**f3**), Br (Fig. 3**f4**), and Ca (Fig. 3**f5**) components in Fig. 3**f** is consistent, which reveals the existence of Ca^{2+} in PQDs. Combined with the element ratio of [Ca]/[Pb] from ICP-OES of 2.26 %, this indicates that the doping level of Ca^{2+} is relatively low. Furthermore, the appearance of Br indicates the successful exchange of halogen ions. Therefore, rational surface doping and halide exchange reaction induced by $CaBr_2$ did not affect the morphology of final $CaBr_2$-$CsPb(Cl/Br)_3$ PQDs.

Furthermore, X-ray photoelectron spectroscopy (XPS) measurements were also carried out. As shown in Fig. 4**a**, Cs, Pb, Cl, Br, and Ca elements can be detected in the XPS test of $CaBr_2$-$CsPb(Cl/Br)_2$ PQDs. Fig. 4**b** reveals that the binding energy of Ca 2p is located at 348.5 and 351.5 eV. While the peaks of Cl 2p and Cs 3d are shifted to higher binding energies in Fig. 4**c, d**. The binding energies of Pb 4f and Br 3d are consistent

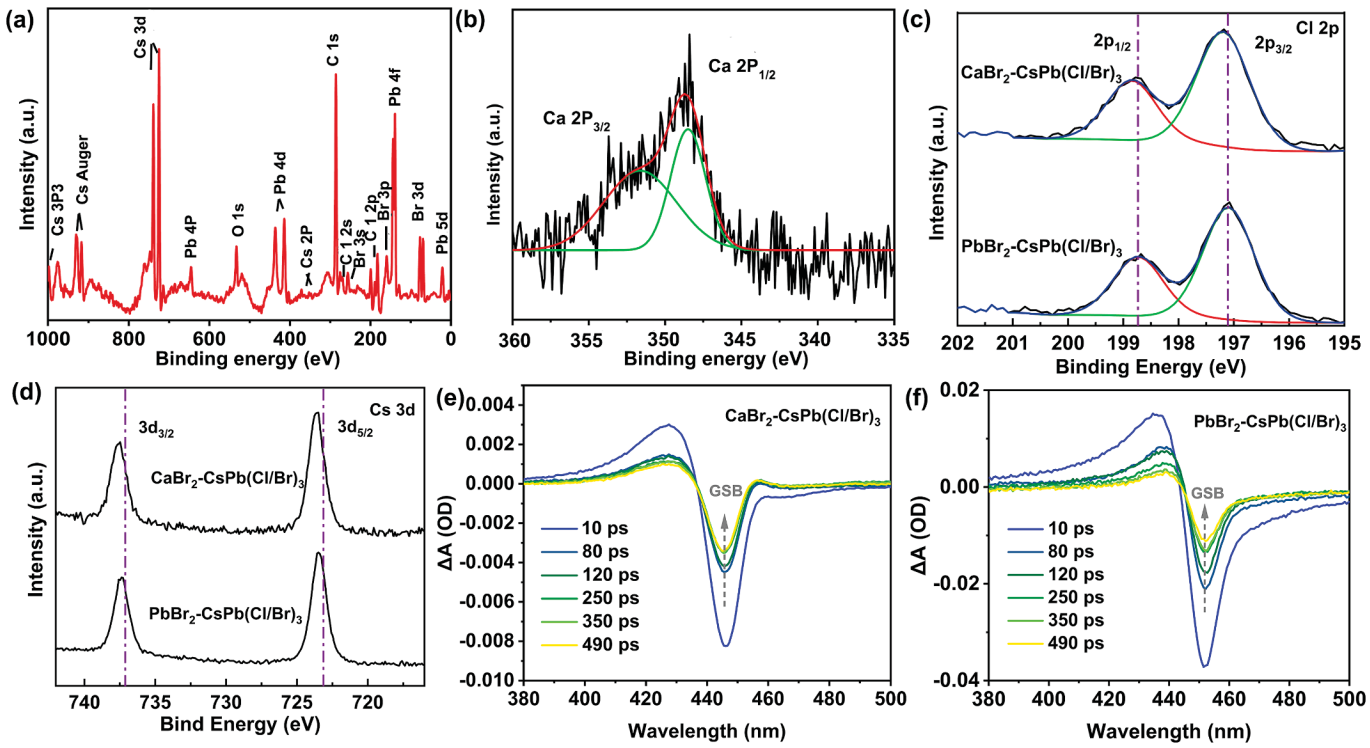

Fig. 4. (a) XPS spectra of $CaBr_2$-$CsPb(Cl/Br)_3$ PQDs. (b) High-resolution XPS spectra of Ca 2p doublet for $CaBr_2$-$CsPb(Cl/Br)_3$ PQDs. High-resolution XPS of (c) Cl 2p and (d) Cs 3d of $CaBr_2$-$CsPb(Cl/Br)_3$ and $PbBr_2$-$CsPb(Cl/Br)_3$ PQDs. TA spectra at different delay times for (e) $CaBr_2$-$CsPb(Cl/Br)_3$ and (f) $PbBr_2$-$CsPb(Cl/Br)_3$ PQDs.

between $PbBr_2$-$CsPb(Cl/Br)_2$ and $CaBr_2$-$CsPb(Cl/Br)_2$ PQDs (**Fig. S8a, b**). It indicates that Ca^{2+} has strong interactions with the other elements of $CaBr_2$-$CsPb(Cl/Br)_2$ PQDs, causing the inhibition of defects. Transient absorption (TA) pump–probe spectroscopy measurements were employed to explore the exciton dynamics of $CaBr_2$-$CsPb(Cl/Br)_3$ and $PbBr_2$-$CsPb(Cl/Br)_3$ PQDs (as displayed in Fig. 4**e, f**). Ground state bleach (GSB) peak of $CaBr_2$-$CsPb(Cl/Br)_3$ PQDs exhibits a slower upward rising rate than $PbBr_2$-$CsPb(Cl/Br)_3$ PQDs, which indicates that $CaBr_2$-$CsPb(Cl/Br)_3$ PQDs is less likely to dissociate into free electrons compared to $PbBr_2$-$CsPb(Cl/Br)_3$ PQDs. Therefore, the introduction of Ca^{2+} can enhance the exciton stability of target $CaBr_2$-$CsPb(Cl/Br)_3$ PQDs.

Generally, cation doping contributes to increasing defect formation energy, thus stabilizing the halogen ions on the PQDs and improving the structural stability of mixed halide PQDs. However, excessive amounts of calcium in the lattice inevitably destroys the lattice and only the proper amount of doping enhances lattice stability. With density functional theory (DFT) calculations, the structure diagram of Cl, Br vacancy, and the defect formation energies of halide in mixed halide PQDs with and without Ca^{2+}-doping conditions was obtained. **Fig. S9a, b** display the structure diagram of Cl and Br vacancy of PQDs with Ca^{2+}-doping. **Fig. S9a1, b1** display the structure diagram of Cl and Br vacancy of PQDs without Ca^{2+}-doping. Comparing the structural diagrams with and without Ca^{2+}-doping, it can be found that PQD without Ca^{2+}-doping exhibit more halogen ion vacancies and dangling bonds than with Ca^{2+}-doping. The defect formation energies of PQDs with/without Ca^{2+}-doping were calculated and listed in **Table S2.** When 1/8 Pb^{2+} is replaced by Ca^{2+}, the defect formation energy of Br-vacancy (3.25 eV) and Cl-vacancy (3.47 eV) are higher than those of $CsPb(Cl/Br)_3$ PQDs (2.81 and 3.21 eV). It indicates the stability of the PQD structure is enhanced when the doping amount of Ca^{2+} is less than 12.5 %, which confirms the positive effect of the doping in this study. The specific calculation process through **Equation S5** can be found in the **SI.**

2.3. Film characteristics of $CaBr_2$-$CsPb(Cl/Br)_3$ and $PbBr_2$-$CsPb(Cl/Br)_3$ PQDs

The optical properties and quality of $CaBr_2$-$CsPb(Cl/Br)_3$ PQD films play a key role in determining the efficiency of the fabricated device. PQD films were spin-coated with Ca_{-430}, Ca_{-450}, Ca_{-467}, Pb_{-430}, Pb_{-450}, and Pb_{-467}. Besides the higher PLQY, $CaBr_2$-$CsPb(Cl/Br)_3$ PQDs are also accompanied by brighter fluorescence-emission than their $PbBr_2$ counterparts as visually observed with our naked eyes in Fig. 5**a–c**. In addition, the stability of these films was also tested. To accelerate the degradation rate, the films were placed in an atmosphere of 30℃ and 80 % relative humidity (RH). The PL intensity of these films at different times and the corresponding photographs under a UV lamp were recorded (**Fig. S10**). **Fig. S10a** illustrates the time-dependent evolution of the films at 80 % RH, where the fluorescence reduction of Pb_{-430} and Pb_{-450} was obvious to the naked eye. The emission of Pb_{-450} is essentially lost after five hours. The corresponding normalized PL intensity was collected and displayed in **Fig. S10b**. With the involvement of calcium, the overall performance of fluorescence intensity is superior to that of the control group without calcium.

To realize deep-blue PeLED, the optimal candidates of Ca_{-450} and Pb_{-450} PQDs were chosen for the stepwise study. The formation process of $CaBr_2$-$CsPb(Cl/Br)_3$ and $PbBr_2$-$CsPb(Cl/Br)_3$ thin films during annealing at 50 ℃ was further investigated via in situ PL spectra (Fig. 5**d, e**). It is observed that Ca_{-450} film exhibits a narrower, more stable, and higher signal intensity emission peak (~448 nm) during annealing, while for Pb_{-450}, the emission PL intensity decays rapidly. This indicates that Ca_{-450} possesses good film-forming properties. As validated by the atomic force microscopy (AFM) characterization (Fig. 5**f, g**), Ca_{-450} gains a smoother surface with a root-mean-square (RMS) of 3.74 nm compared to that of Pb_{-450} film (4.37 nm), which facilitates interfacial charge transfer. Additionally, hole-only devices with the structure of indium tin oxide (ITO) / poly(ethylene dioxythiophene): polystyrene sulfonate (PEDOT: PSS) / poly(9-vinyl carbazole) (PVK) / PQDs / MoO_3 / Au were prepared to estimate the trap state densities (N_t). According to **Equation**

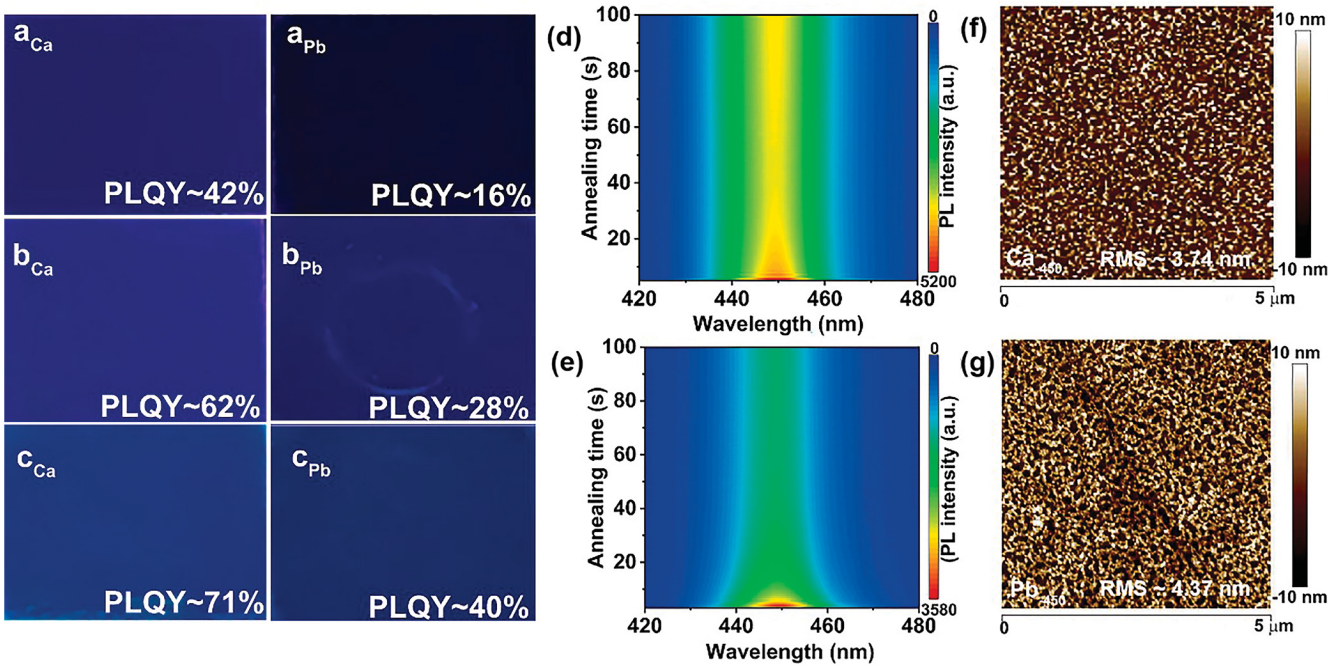

Fig. 5. (a, b, c) Films of Ca_{-430} & Pb_{-430}, Ca_{-450} & Pb_{-450}, and Ca_{-467} & Pb_{-467} photos under UV light. Heat maps of spectrally resolved photoluminescence (PL) measured during (d) Ca_{-450} and (e) Pb_{-450} films at the annealing temperature of 50 °C. AFM images of (f) Ca_{-450} and (g) Pb_{-450}.

S6 & S7 and dark current–voltage measurements (**Figs. S11, 12**), $CaBr_2$-$CsPb(Cl/Br)_3$ PQDs merits a lower defect density of 4.53×10^{17} cm^{-3} than that of $PbBr_2$-$CsPb(Cl/Br)_3$ PQDs (5.34×10^{17} cm^{-3}). Consequently, the defects of $CaBr_2$-$CsPb(Cl/Br)_3$ PQDs have been efficaciously repaired.

Removing excess ligands while maintaining a good crystal structure is conducive to charge injection, thereby favoring efficient PeLEDs. Here, the stability and robustness of blue PQDs washed by anti-solvent were evaluated. The precipitation and redispersion process was repeated 2 times, in which methyl acetate was used as the anti-solvent to wash the PQDs. Generally, the PL intensity decreases with the absence of ligands, however, the PL intensity of $CaBr_2$-$CsPb(Cl/Br)_3$ PQDs did not decrease but increased after the first round of washing, as illustrated in **Fig. S13a**. It indicates that the removal of excessive $CaBr_2$ is beneficial to the radiative luminescence of PQDs and the involved Ca^{2+} helps the crystal to maintain structural integrity, which agrees with the DFT

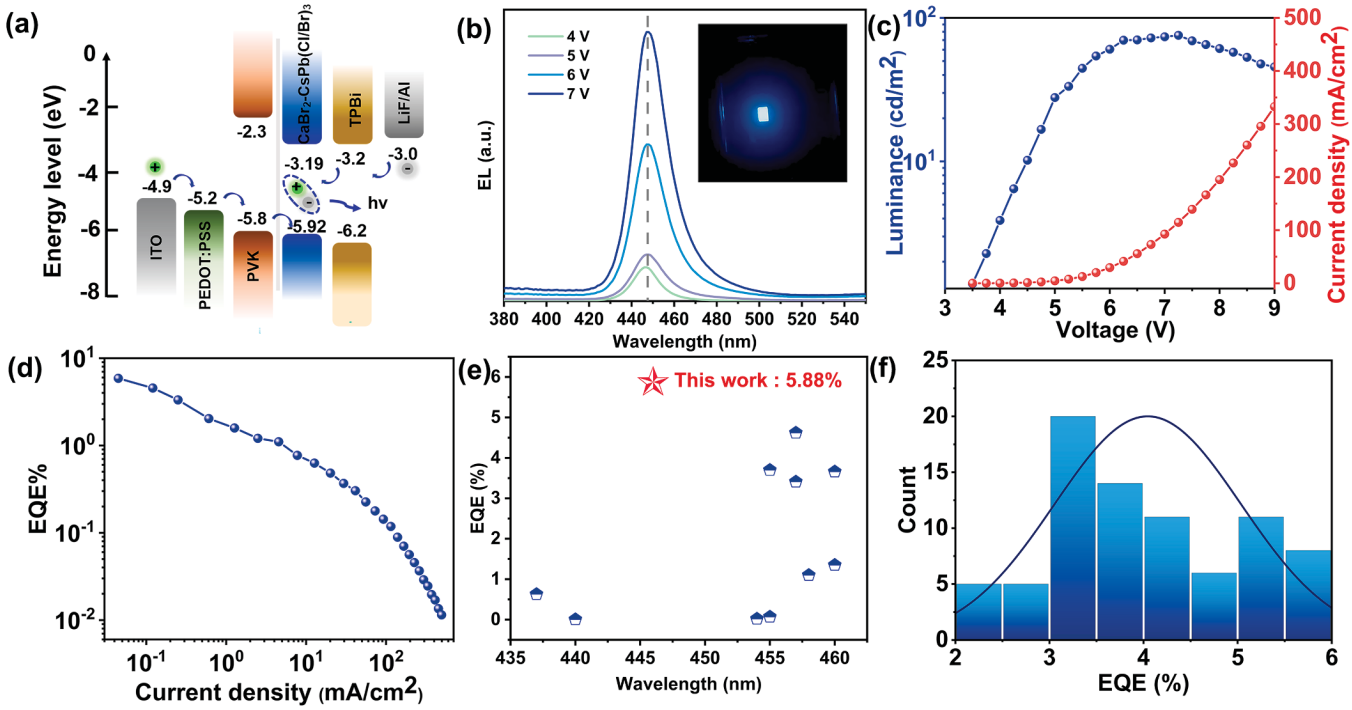

Fig. 6. Device structure and performance characteristics of efficient deep-blue $CaBr_2$-$CsPb(Cl/Br)_3$ PQDs light emitting diodes. (a) Schematic illustration of band energies and architecture. (b) Electroluminescence spectra driven by voltages from 4 to 7 V. Inset image show the luminescence of device. (c) (J-V-L) and (d) EQE characteristics (e) Comparison of our work with the other deep-blue PeLEDs. (f) Histogram of peak EQEs measured from 80 devices.

calculation result that the introduction of an appropriate amount of Ca^{2+} can enhance the formation barrier of halogen vacancies. After the second round of washing, a slight PL intensity decrease was observed. In comparison, the PL intensity of $PbBr_2$-$CsPb(Cl/Br)_3$ PQDs undergoes a decrease of more than 80 % at the outset of washing (**Fig. S13b**). The results demonstrate that the addition of $CaBr_2$ creates a Br-rich environment for $CaBr_2$-$CsPb(Cl/Br)_3$ PQDs and reduces Cl vacancy, which is consistent with the XPS result that Ca^{2+} interacts with halogens and can inhibit the formation of defects during the ligand washing.

2.4. PeLEDs

The device structure of PeLED is ITO / Poly(3,4-ethylenedioxythiophene) /poly(styrenesulfonate) (PEDOT: PSS) / Poly (N-vinyl carbazole) (PVK) / PQDs / (1,3,5-Tris(1-phenyl-1H-benzimidazol-2-yl)benzene) (TPBi) / LiF / Al, as shown in Fig. 6**a**. The valence band (VB) of $CaBr_2$-$CsPb(Cl/Br)_3$ and $PbBr_2$-$CsPb(Cl/Br)_3$ PQDs were obtained by ultra-violet photoelectron spectroscopy (UPS) (**Fig. S14**). VB E_v of $CaBr_2$-$CsPb(Cl/Br)_3$ and $PbBr_2$-$CsPb(Cl/Br)_3$ PQDs are −5.92 and −7.62 eV, which were calculated by **Equation S8**. The corresponding bandgap was obtained by Tauc plots (**Fig. S15**). The conduction band (CB) E_c of $CaBr_2$-$CsPb(Cl/Br)_3$ and $PbBr_2$-$CsPb(Cl/Br)_3$ PQDs are −3.19 and −4.89 eV, respectively. These results suggest that calcium-modified $CsPb(Cl/Br)_3$ PQDs have better energy level matching than $PbBr_2$-$CsPb(Cl/Br)_3$ PQDs. **Fig. S16** reveals the EL spectra of $PbBr_2$-$CsPb(Cl/Br)_3$ PQDs device suffered a larger redshift of 4 nm from 448 to 452 nm, however, $CaBr_2$-$CsPb(Cl/Br)_3$ PeLED bore a relatively stable EL spectra at 447 nm from 4 ~ 7 V and 450 nm under 8 V voltage, respectively. Additionally, the CIE of $CaBr_2$-$CsPb(Cl/Br)_3$ shows a smaller vertical coordinate than $PbBr_2$-$CsPb(Cl/Br)_3$ PeLED. The change of CIE is caused by the phase separation and ion migration with the increase of electric field intensity. Therefore, the introduction of Ca^{2+} effectively inhibits ion migration and phase separation at low voltage (4 ~ 7 V). The J–V–L characteristics can be found in **Fig. S17**, $CaBr_2$-$CsPb(Cl/Br)_3$ PeLED has a lower turn-on voltage (V_{on} ~ 3.75 V), compared to the $PbBr_2$-$CsPb(Cl/Br)_3$ PeLED, which benefits from the superior energy levels matching. An enhanced maximum luminance of 141.7 cd/m^2 of the $CaBr_2$-$CsPb(Cl/Br)_3$ and 30.1 cd/m^2 of $PbBr_2$-$CsPb(Cl/Br)_3$ PeLEDs, meanwhile, the corresponding current efficiency of 1.29 and 0.29 cd/A are shown in **Fig. S18**. **Fig. S19** illustrates the EQE of those two PeLEDs are 3.39 % and 0.43 %, respectively. At the same time, the other two sets of emission peak corresponding devices were also fabricated. **Fig. S20** shows the performance characteristics of $CaBr_2$-$CsPb(Cl/Br)_3$ and $PbBr_2$-$CsPb(Cl/Br)_3$ PeLEDs peaked at 470 nm. $CaBr_2$-$CsPb(Cl/Br)_3$ PeLED has relatively stable EL spectra at 470 nm with the applied voltage from 4 to 8 V (**Fig. S20a**), however, **Fig. S20a1** shows $PbBr_2$-$CsPb(Cl/Br)_3$ PeLEDs generating a redshift from 471 to 473 nm under applied voltage from 4 to 7 V. It indicates that $CaBr_2$-$CsPb(Cl/Br)_3$ PQDs can effectively avoid the formation of deep defects, to improve the device performance. From the plots of J–V–L (**Fig. S20b and b1**), the maximum brightness of the device is 63.50 cd/m^2 with $CaBr_2$-$CsPb(Cl/Br)_3$ PQDs and 112.90 cd/m^2 with $PbBr_2$-$CsPb(Cl/Br)_3$ PQDs. The corresponding current efficiency is 4.00 and 1.43 cd/A, respectively. The maximum EQE of those PeLEDs reachs 6.15 % (470 nm) and 2.08 % (473 nm), respectively (**Fig. S20c and c1**). PL of 430 nm emitting PQDs device were also fabricated. Unfortunately, due to the deep energy level of this emission wavelength PQDs, it affects the carrier injection leading to ineffective electrospectral (**Fig. S21**).

Based on maintaining the original structure of the PQDs, the more ligands are removed, the better for carrier injection in the device. To obtain more efficient deep-blue PeLEDs, trace water is introduced as an auxiliary treatment method to further remove the excessive ligands. Powder XRD patterns collected from the films of Ca-$_{446}$ and Pb-$_{446}$ PQDs (**Fig. S22**) show the same peak location and different intensities of those samples. It confirmed the crystal structure was retained after water was introduced into the purification of the PQD. Additionally, the intensity of Ca-$_{446}$ is higher than that of Pb-$_{446}$ PQDs indicating that PQDs acquired a higher crystalline phase content by introducing Ca^{2+}. XPS measurements were carried out to analyze the amount of ligands, **Fig. S23** shows the integrated areas of the C and N peaks of parent, vapour and water treated $CaBr_2$-$CsPb(Cl/Br)_3$ PQDs. According to the value of integrated areas of the C and N peaks, the atomic concentration of N (n_N) was calculated to be 0.33 of the parent, 0.30 of vapour, and 0.30 of liquid water treated, respectively by **Equation S4**. The decreased n_N value from 0.33 to 0.30 indicates that excessive ligands can be fully removed with trace water. Finally, the target $CaBr_2$-$CsPb(Cl/Br)_3$ PQDs-based PeLED has relatively stable EL spectra at 447 nm, producing a one-nanometer redshift compared to PL spectra (Fig. 6**b**). It indicates that $CaBr_2$-$CsPb(Cl/Br)_3$ PQDs can effectively avoid the formation of deep defects and improve the device's performance. The EL intensity of $CaBr_2$-$CsPb(Cl/Br)_3$ PeLED increases with the increase of the applied voltage from 4 to 7 V. CIE of $CaBr_2$-$CsPb(Cl/Br)_3$ PeLED is (0.159, 0.018). From the plots of current density/ luminance versus voltage curves (J/L-V, Fig. 6**c**), the device of $CaBr_2$-$CsPb(Cl/Br)_3$ PQDs exhibits a maximum brightness of 75.6 cd/m^2. The corresponding current efficiency is 3.28 cd/A (**Fig. S24**). In Fig. 6**d**, the maximum EQE of deep-blue PeLED based on $CaBr_2$-$CsPb(Cl/Br)_3$ PQDs reaches 5.88 %, which is superior to others among the deep-blue territory (<460 nm) **(**Fig. 6**e** and **Table S3**). Fig. 6**f** shows the average efficiency histogram acquired from 80 devices, and the average EQE is 4.04 %, which confirms the reproducibility of our rational design.

3. Conclusion

In summary, a series of deep blue emitting $CaBr_2$-$CsPb(Cl/Br)_3$ PQDs were successfully developed through **FAECDIP** method bearing the merits of simultaneous ion-exchange and Ca^{2+} doping. Compared with the control group ($PbBr_2$-$CsPb(Cl/Br)_3$ PQDs), the close BDE and smaller ionic radius of Ca^{2+} allow for the quick preparation of high-quality blue PQDs. Ca^{2+} achieves an increase in the reaction rate of 1.6 times compared to Pb^{2+}. The introduction of Ca^{2+} successfully passivates the defects of PQDs and enhances the exciton binding energy, which favors structural stability and carrier transportation. Target PQDs were made with PL spectra that could be reversibly tuned from 402 to 500 nm. Consequently, $CaBr_2$-$CsPb(Cl/Br)_3$ PQDs exhibited a maximum PLQY of 80.3 % at 446 nm. Corresponding deep-blue $CsPb(Cl/Br)_3$ PeLED with a record EQE of 5.88 % (at 447 nm) along with the CIE coordinates of (0.158, 0.018) was achieved. The average EQE of 4.04 % and steady EL spectrum were also obtained. This approach provides a strategy to broaden the color spectrum and encourages the application of mixed halide perovskites in deep-blue PeLEDs in the future.

CRediT authorship contribution statement

Jing Zhou: Writing – original draft, Methodology, Investigation, Formal analysis, Data curation, Conceptualization. **Hongli Liu:** Writing – review & editing, Visualization, Supervision, Resources, Conceptualization. **Sisi Wang:** Writing – review & editing, Software, Methodology, Formal analysis. **Longfei Yuan:** Software. **Narjes Dridi:** Writing – review & editing. **Shirong Wang:** Supervision, Resources, Funding acquisition. **Hedi Mattoussi:** Writing – review & editing, Resources, Project administration, Funding acquisition, Formal analysis. **Xianggao Li:** Writing – review & editing, Supervision, Software, Funding acquisition.

Declaration of competing interest

The authors declare that they have no known competing financial interests or personal relationships that could have appeared to influence the work reported in this paper.

Data availability

Data will be made available on request.

Acknowledgments

This work was supported by the National Key Research and Development Program of China (2022YFB3603003), the National Science Foundation (NSF-CHE #1508501and #2005079), and AFOSR (Grant No. FA9550-18-1- 0144). The authors thank their financial support. J.Z. thanks the China Scholarship Council (CSC) for financial support from fellowship No. 201906250003.

Appendix A. Supplementary data

Supplementary data to this article can be found online at https://doi.org/10.1016/j.cej.2024.151227.

References

[1] H.J. Cho, S.H. Park, M.H. Kim, Y.H. Wolf, C. Lee, C.J.H.S.L. Heo, A. Myoung, N. Yoo, S. Im, S.H. Friend, T.W.R.H. Lee, Overcoming the electroluminescence efficiency limitations of perovskite light-emitting diodes, Science 350 (6265) (2015) 1222–1225.

[2] Y. Cao, N. Wang, H. Tian, J. Guo, Y. Wei, H. Chen, Y. Miao, W. Zou, K. Pan, Y. He, H. Cao, Y. Ke, M. Xu, Y. Wang, M. Yang, K. Du, Z. Fu, D. Kong, D. Dai, Y. Jin, G. Li, H. Li, Q. Peng, J. Wang, W. Huang, Perovskite light-emitting diodes based on spontaneously formed submicrometre-scale structures, Nature 562 (2018) 249–253, https://doi.org/10.1038/s41586-018-0576-2.

[3] T. Chiba, Y. Hayashi, H. Ebe, K. Hoshi, J. Sato, S. Sato, Y.-J. Pu, S. Ohisa, J. Kido, Anion-exchange red perovskite quantum dots with ammonium iodine salts for highly efficient light-emitting devices, Nat. Photonics 12 (2018) 681–687, https://doi.org/10.1038/s41566-018-0260-y.

[4] K. Lin, J. Xing, L.N. Quan, F.P.G. de Arquer, X. Gong, J. Lu, L. Xie, W. Zhao, D. Zhang, C. Yan, W. Li, X. Liu, Y. Lu, J. Kirman, E.H. Sargent, Q. Xiong, Z. Wei, Perovskite light-emitting diodes with external quantum efficiency exceeding 20 percent, Nature 562 (2018) 245–248, https://doi.org/10.1038/s41586-018-0575-3.

[5] L.P. Maksym, V. Kovalenko, M.I. Bodnarchuk, Properties and potential optoelectronic applications of lead halide perovskite nanocrystals, Science 358 (2017) 5.

[6] Z. Ning, X. Gong, R. Comin, G. Walters, F. Fan, O. Voznyy, E. Yassitepe, A. Buin, S. Hoogland, E.H. Sargent, Quantum-dot-in-perovskite solids, Nature 523 (2015) 324–328, https://doi.org/10.1038/nature14563.

[7] X. Mei, D. Jia, J. Chen, S. Zheng, X. Zhang, Approaching high-performance light-emitting devices upon perovskite quantum dots: Advances and prospects, Nano Today 43 (2022), https://doi.org/10.1016/j.nantod.2022.101449.

[8] Z. Chen, Z. Li, T.R. Hopper, A.A. Bakulin, H.L. Yip, Materials, photophysics and device engineering of perovskite light-emitting diodes, Rep. Prog. Phys. 84 (4) (2021), https://doi.org/10.1088/1361-6633/abefba.

[9] X.K. Liu, W. Xu, S. Bai, Y. Jin, J. Wang, R.H. Friend, F. Gao, Metal halide perovskites for light-emitting diodes, Nat. Mater. 20 (1) (2021) 10–21, https://doi.org/10.1038/s41563-020-0784-7.

[10] W. Bai, T. Xuan, H. Zhao, H. Dong, X. Cheng, L. Wang, R.J. Xie, Perovskite Light-Emitting Diodes with an External Quantum Efficiency Exceeding 30%, Adv. Mater. (2023) https://doi.org/10.1002/adma.202302283.

[11] J. Jiang, Z. Chu, Z. Yin, J. Li, Y. Yang, J. Chen, J. Wu, J. You, X. Zhang, Red perovskite light-emitting diodes with efficiency exceeding 25% realized by co-spacer cations, Adv. Mater. 34 (36) (2022), https://doi.org/10.1002/adma.202204460.

[12] D. Yang, X. Li, W. Zhou, S. Zhang, C. Meng, Y. Wu, Y. Wang, H. Zeng, $CsPbBr_3$ Quantum Dots 2.0: Benzenesulfonic Acid Equivalent Ligand Awakens Complete Purification, Adv. Mater. 31 (30) (2019) e1900767.

[13] F. Liu, Y. Zhang, C. Ding, S. Kobayashi, T. Izuishi, N. Nakazawa, T. Toyoda, T. Ohta, S. Hayase, T. Minemoto, K. Yoshino, S. Dai, Q. Shen, Highly Luminescent Phase-Stable $CsPbI_3$ Perovskite Quantum Dots Achieving Near 100% Absolute Photoluminescence Quantum Yield, ACS Nano 11 (10) (2017) 10373–10383, https://doi.org/10.1021/acsnano.7b05442.

[14] F. Yang, H. Chen, R. Zhang, X. Liu, W. Zhang, J. Zhang, F. Gao, L. Wang, Efficient and spectrally stable blue perovskite light-emitting diodes based on potassium passivated nanocrystals, Adv. Funct. Mater. 30 (2020), https://doi.org/10.1002/adfm.201908760.

[15] W. Yin, M. Li, W. Dong, Z. Luo, Y. Li, J. Qian, J. Zhang, W. Zhang, Y. Zhang, S. V. Kershaw, X. Zhang, W. Zheng, A.L. Rogach, Multidentate Ligand Polyethylenimine Enables Bright Color-Saturated Blue Light-Emitting Diodes Based on $CsPbBr_3$ Nanoplatelets, ACS Energy Lett. 6 (2) (2021) 477–484, https://doi.org/10.1021/acsenergylett.0c02651.

[16] J. Dong, F. Lu, D. Han, J. Wang, Z. Zang, L. Kong, Y. Zhang, X. Ma, J. Zhou, H. Ji, X. Yang, N. Wang, Deep-blue electroluminescence of perovskites with reduced dimensionality achieved by manipulating adsorption-energy differences, Angew. Chem. Int. Ed. 61 (40) (2022) e202210322.

[17] Z. Yuan, Y. Shu, Y. Tian, Y. Xin, B. Ma, A facile one-pot synthesis of deep blue luminescent lead bromide perovskite microdisks, Chem. Commun. (camb.) 51 (91) (2015) 16385–16388, https://doi.org/10.1039/c5cc06750b.

[18] Y. Gao, C. Luo, C. Yan, W. Li, C. Liu, W. Yang, Copper-doping defect-lowered perovskite nanosheets for deep-blue light-emitting diodes, J. Colloid Interface Sci. 607 (Pt 2) (2022) 1796–1804, https://doi.org/10.1016/j.jcis.2021.09.061.

[19] S. Parveen, P.K. Prasanna, S. Chakraborty, P.K. Giri, Stable deep blue emission with unity quantum yield in organic–inorganic halide perovskite 2D nanosheets doped with cerium and terbium at high concentrations, J. Mater. Chem. C 9 (7) (2021) 2437–2454, https://doi.org/10.1039/d0tc04937a.

[20] S. Yuan, Z.K. Wang, L.X. Xiao, C.F. Zhang, S.Y. Yang, B.B. Chen, H.T. Ge, Q.S. Tian, Y. Jin, L.S. Liao, Optimization of low-dimensional components of quasi-2D perovskite films for deep-blue light-emitting diodes, Adv. Mater. 31 (44) (2019) e1904319.

[21] A.K. Guria, S.K. Dutta, S.D. Adhikari, N. Pradhan, Doping Mn^{2+} in lead halide perovskite nanocrystals: successes and challenges, ACS Energy Lett. 2 (2017) 1014–1021, https://doi.org/10.1021/acsenergylett.7b00177.

[22] C. Bi, S. Wang, Q. Li, S.V. Kershaw, J. Tian, A.L. Rogach, Thermally Stable Copper (II)-Doped Cesium Lead Halide Perovskite Quantum Dots with Strong Blue Emission, J. Phys. Chem. Lett. 10 (2019) 943–952, https://doi.org/10.1021/acs.jpclett.9b00290.

[23] S. Hou, M.K. Gangishetty, Q. Quan, D.N. Congreve, Efficient blue and white perovskite light-emitting diodes via manganese doping, Joule 2 (2018) 2421–2433, https://doi.org/10.1016/j.joule.2018.08.005.

[24] S. Zou, G. Yang, T. Yang, D. Zhao, Z. Gan, W. Chen, H. Zhong, X. Wen, B. Jia, B. Zou, Template-free synthesis of high-yield fe-doped cesium lead halide perovskite ultralong microwires with enhanced two-photon absorption, J. Phys. Chem. Lett. 9 (2018) 4878–4885, https://doi.org/10.1021/acs.jpclett.8b02127.

[25] Y. Xie, B. Peng, I. Bravic, Y. Yu, Y. Dong, R. Liang, Q. Ou, B. Monserrat, S. Zhang, Highly Efficient Blue-Emitting $CsPbBr_3$ Perovskite Nanocrystals through Neodymium Doping, Adv. Sci. 7 (2020) 2001698, https://doi.org/10.1002/advs.202001698.

[26] Y. Yang, S. Xu, Z. Ni, C.H. Van Brackle, L. Zhao, X. Xiao, X. Dai, J. Huang, Highly efficient pure-blue light-emitting diodes based on rubidium and chlorine alloyed metal halide perovskite, Adv. Mater. (2021) e2100783.

[27] Q. Cao, A. Ilyas, S. Zhang, Z. Ju, F. Sun, T. Liu, Y.M. Yang, Y. Lu, X. Liu, R. Deng, Lanthanide-doping enables kinetically controlled growth of deep-blue two-monolayer halide perovskite nanoplatelets, Nanoscale 13 (2021) 11552–11560, https://doi.org/10.1039/d1nr02508b.

[28] Y.H. Zhou, C. Wang, S. Yuan, C. Zou, Z. Su, K.L. Wang, Y. Xia, B. Wang, D. Di, Z. K. Wang, L.S. Liao, Stabilized low-dimensional species for deep-blue perovskite light-emitting diodes with EQE approaching 3.4%, J. Am. Chem. Soc. (2022) https://doi.org/10.1021/jacs.2c07172.

[29] L. G.P. Nedelcu, S. Yakunin, M.I. Bodnarchuk, M.J. Grotevent, M.V. Kovalenko, Fast Anion-Exchange in Highly Luminescent Nanocrystals of Cesium Lead Halide Perovskites ($CsPbX_3$, X = Cl, Br, I), Nano Lett. 15 (2015) 5635–5640, https://doi.org/10.1021/acs.nanolett.5b02404.

[30] F. Zhang, X. Zhang, C. Wang, M. Sun, X. Luo, Y. Yang, S. Chang, D. Zhang, L. Duan, Chlorine distribution management for spectrally stable and efficient perovskite blue light-emitting diodes, Nano Energy 79 (2021), https://doi.org/10.1016/j.nanoen.2020.105486.

[31] X. Liu, E. Mei, Z. Liu, J. Du, X. Liang, W. Xiang, Stable, Low-Threshold Amplification Spontaneous Emission of Blue-Emitting $CsPbCl_2Br_1$ Perovskite Nanocrystals Glasses with Controlled Crystallization, ACS Photonics 8 (2021) 887–893, https://doi.org/10.1021/acsphotonics.0c01904.

[32] Y.J. Yoon, Y.S. Shin, H. Jang, J.G. Son, J.W. Kim, C.B. Park, D. Yuk, J. Seo, G. H. Kim, J.Y. Kim, Highly Stable Bulk Perovskite for Blue LEDs with Anion-Exchange Method, Nano Lett. 21 (2021) 3473–3479, https://doi.org/10.1021/acs.nanolett.1c00124.

[33] M. Karlsson, Z. Yi, S. Reichert, X. Luo, W. Lin, Z. Zhang, C. Bao, R. Zhang, S. Bai, G. Zheng, P. Teng, L. Duan, Y. Lu, K. Zheng, T. Pullerits, C. Deibel, W. Xu, R. Friend, F. Gao, Mixed halide perovskites for spectrally stable and high-efficiency blue light-emitting diodes, Nat. Commun. 12 (2021) 361, https://doi.org/10.1038/s41467-020-20582-6.

[34] Q. Jing, M. Zhang, X. Huang, X. Ren, P. Wang, Z. Lu, Surface passivation of mixed-halide perovskite $CsPb(Br_xI_{1-x})_3$ nanocrystals by selective etching for improved stability, Nanoscale 9 (2017) 7391–7396, https://doi.org/10.1039/c7nr01287j.

[35] J. Hieulle, X. Wang, C. Stecker, D.Y. Son, L. Qiu, R. Ohmann, L.K. Ono, A. Mugarza, Y. Yan, Y. Qi, Unraveling the Impact of Halide Mixing on Perovskite Stability, J. Am. Chem. Soc. 141 (2019) 3515–3523, https://doi.org/10.1021/jacs.8b11210.

[36] Y. Shen, K.C. Shen, Y.Q. Li, M. Guo, J. Wang, Y. Ye, F.M. Xie, H. Ren, X. Gao, F. Song, J.X. Tang, Interfacial Potassium-Guided Grain Growth for Efficient Deep-Blue Perovskite Light-Emitting Diodes, Adv. Funct. Mater. 31 (6) (2020), https://doi.org/10.1002/adfm.202006736.

[37] C. Yan, C. Luo, W. Li, X. Peng, J. Cao, X. Zeng, Y. Gao, X. Fu, X. Chu, W. Deng, F. Chun, S. Yang, Q. Wang, W. Yang, Thermodynamics-Induced Injection Enhanced Deep-Blue Perovskite Quantum Dot LEDs, ACS Appl. Mater. Interfaces 13 (48) (2021) 57560–57566, https://doi.org/10.1021/acsami.1c16428.

[38] Z.J. Yong, S.Q. Guo, J.P. Ma, J.Y. Zhang, Z.Y. Li, Y.M. Chen, B.B. Zhang, Y. Zhou, J. Shu, J.L. Gu, L.R. Zheng, O.M. Bakr, H.T. Sun, Doping-Enhanced Short-Range Order of Perovskite Nanocrystals for Near-Unity Violet Luminescence Quantum Yield, J. Am. Chem. Soc. 140 (31) (2018) 9942–9951, https://doi.org/10.1021/jacs.8b04763.

[39] S. Zhang, H. Liu, X. Li, S. Wang, Enhancing quantum yield of $CsPb(Br_xCl_{1-x})_3$ nanocrystals through lanthanum doping for efficient blue light-emitting diodes, Nano Energy 77 (2020), https://doi.org/10.1016/j.nanoen.2020.105302.
[40] W. Zhang, X. Li, C. Peng, F. Yang, L. Lian, R. Guo, J. Zhang, L. Wang, $CsPb(Br/Cl)_3$ Perovskite Nanocrystals with Bright Blue Emission Synergistically Modified by Calcium Halide and Ammonium Ion, Nanomaterials 12 (12) (2022), https://doi.org/10.3390/nano12122026.
[41] G. Huang, C. Wang, S. Xu, S. Zong, J. Lu, Z. Wang, C. Lu, Y. Cui, Postsynthetic Doping of $MnCl_2$ Molecules into Preformed $CsPbBr_3$ Perovskite Nanocrystals via a Halide Exchange-Driven Cation Exchange, Advanced Materials 29 (29) (2017), https://doi.org/10.1002/adma.201700095.
[42] L. Protesescu, S. Yakunin, M.I. Bodnarchuk, F. Krieg, R. Caputo, C.H. Hendon, R. X. Yang, A. Walsh, M.V. Kovalenko, Nanocrystals of Cesium Lead Halide Perovskites ($CsPbX_3$, X = Cl, Br, and I): Novel Optoelectronic Materials Showing Bright Emission with Wide Color Gamut, Nano Lett. 15 (6) (2015) 3692–3696, https://doi.org/10.1021/nl5048779.
[43] V.G.V. Dutt, S. Akhil, N. Mishra, Fast, tunable and reversible anion-exchange in $CsPbBr_3$ perovskite nanocrystals with hydrohalic acids, CrystEngComm 22 (30) (2020) 5022–5030, https://doi.org/10.1039/d0ce00722f.
[44] J.K. YR Luo, CRC handbook of chemistry and physics, notendur.hi.is (2012) 65-98.
[45] G. Zhang, R. Long, Y. Lu, S. Zhang, W. Zhao, Y. Yu, Q. Mi, P. Qin, F. Huang, Calcium-Assisted In Situ Formation of Perovskite Nanocrystals for Luminescent Green and Blue Emitters, ACS Applied Nano Materials 4 (12) (2021) 14303–14311, https://doi.org/10.1021/acsanm.1c03937.